

# Detachment in conventional and advanced Double-Null plasmas in TCV

O. Février<sup>1</sup>, C. Theiler<sup>1</sup>, S. Coda<sup>1</sup>, C. Colandrea<sup>1</sup>, H. de Oliveira<sup>1</sup>, B. P. Duval<sup>1</sup>, S. Gorno<sup>1</sup>, B. Labit<sup>1</sup>, B. Linehan<sup>2</sup>, R. Maurizio<sup>1</sup>, A. Perek<sup>3</sup>, H. Reimerdes<sup>1</sup>, C. Wüthrich<sup>1</sup>, the TCV Team<sup>a</sup>

<sup>1</sup>École Polytechnique Fédérale de Lausanne (EPFL), Swiss Plasma Center (SPC), CH-1015 Lausanne, Switzerland.

<sup>2</sup>Plasma Science and Fusion Center MIT, Cambridge, Massachusetts 02139, USA.

<sup>3</sup>Dutch Institute for Fundamental Energy Research, De Zaale 20, 5612 AJ Eindhoven, Netherlands.

<sup>a</sup>See the author list of S. Coda et al 2019 *Nucl. Fusion* **59** 112023.

E-mail: [olivier.fevrier@epfl.ch](mailto:olivier.fevrier@epfl.ch)

**Abstract.** Divertor detachment is investigated on the Tokamak à Configuration Variable (TCV) for conventional and alternative Double-Null (DN) magnetic geometries in L-Mode, Ohmic density ramps and then compared to precisely matched Single-Null (SN) geometries. The poloidal flux expansion at the outer strikepoint(s) is varied by a factor 2 and the total flux expansion by 30% in LSN and DN configurations. Leg power sharing for DN and near-DN in attached conditions is in line with previous studies in other devices, with balanced power partition between upper and lower divertor achieved for  $|\delta R_{sep}| \lesssim \lambda_q/2$ . This results in a reduction in the lower outer target integral and peak heat flux compared to a LSN by 30%. Unlike previous studies,  $\lambda_q$  is fairly insensitive to  $\delta R_{sep}$ . The detachment threshold in these geometries is investigated from target measurements with wall-embedded Langmuir probes and two-dimensional CIII line emissivity profiles across the two divertor regions. DN plasmas display clear benefits compared to their LSN counterparts. Transitioning from a LSN to DN shows a substantial reduction, of approx. 20-25%, in the detachment threshold for the active divertor legs as well as a 50% higher radiated fraction at all  $\langle n_e \rangle$ . The density limit is simultaneously reduced in DN by 10%–20%. Across the explored range, poloidal flux expansion has only a small effect on the detachment threshold in LSN (as seen in previous experiments), and no effect in DN, with similar observations for the total flux expansion. In general, no strong benefits of increased poloidal or total flux expansion are observed across the explored range.

This is an author-created, un-copyedited version of an article accepted for publication in Nuclear Fusion. Neither the IAEA nor IOP Publishing Ltd is responsible for any errors or omissions in this version of the manuscript and/or any version derived from it. The Version of Record is available online at <https://doi.org/10.1088/1741-4326/ac27c6>.

PACS numbers:

## 1. Introduction

The high power levels crossing the separatrix of magnetically confined fusion plasmas, in combination with a narrow Scrape-off Layer (SOL) width [1], make the task of staying within acceptable target heat loads extremely challenging for fusion reactors. Material limits set the upper limit of the target heat fluxes to  $10 - 20 \text{ MW/m}^2$  [2, 3, 4] for steady-state conditions. If unmitigated, target heat fluxes in ITER and DEMO are expected to be well above this value [5, 6]. Such mitigation will require operation in a detached regime [7, 8, 9], where most of the exhausted heat is dissipated through radiation, and the plasma pressure along the field lines in the SOL develops strong parallel gradients, allowing access to low temperatures (below 5 eV) and low particle fluxes at the targets [10, 9]. Detachment is, however, associated with a cold radiative front that can move along the leg from the target plates up to the X-point and further into the confined plasma, potentially resulting in confinement degradation or disruption [11]. In recent years, significant effort has been dedicated in developing advanced divertor configurations that can facilitate the mitigation of the target heat fluxes and in obtaining detached regimes compatible with continued high core performance. For this purpose, configurations such as the Super-X [12], the X-Divertor [13] or the Snowflake [14] have been proposed. However, these advanced magnetic geometries generally address only the outer divertor leg performance, whilst in a reactor, significant heat fluxes will also impinge upon the inner targets. This issue can be addressed by a Double-Null (DN) configuration. By magnetically separating the outer and the inner SOL, DN configurations allow power sharing between two outer legs, and, possibly, with two radiation fronts. Advanced divertor geometries may then be applied to both active legs, further increasing the expected benefits. In addition, depending upon the degree of balance of the DN configuration, exhaust can be equally distributed between the two exhaust legs, whereas SN (Single-Nulls) configurations typically favor one leg. DN configurations are being considered for several reactor concepts, such as the European DEMO [15, 16], the Korean K-DEMO [17] or ARC [18].

DN configurations were explored in several devices such as Alcator C-Mod [19], DIII-D [20, 21, 22], EAST [23] and MAST [24]. A main focus of these studies was,

in general, the sharing of power between the divertor legs as a function of the distance  $\delta R_{sep}$  between the two magnetic separatrices mapped to the outer mid-plane. In Alcator C-Mod [19] and DIII-D [20], it was found that the balance of heat flux going to the upper and lower divertors was well fit by a hyperbolic tangent function. In [19], based upon analytical considerations and experimental data, the authors show that, in L- and I-mode, the balance actually follows a logistic function of  $\delta R_{sep}$ . In terms of heat flux profiles, one of the main parameters is the heat flux decay length,  $\lambda_q$  [1], which was seen in DIII-D to be insensitive to the magnetic balance far from the DN configuration, and to have a complex dependency close to an ideal DN configuration, depending on the observed divertor.

This article focuses upon a comparison of divertor characteristics (in terms of heat fluxes and detachment access) of SN and DN configurations, in standard and alternative configurations on the TCV tokamak. It is organized as follow. In section 2, we describe the experimental setup and introduce the main diagnostics used in this study. We then investigate in section 3 the effect of the balance of the DN configurations on the power exhaust properties, namely the power sharing between the divertors and  $\lambda_q$ . In section 4, we explore detachment in DN configurations, that are compared to detachment in similar SN, both in a conventional geometry, an X-Divertor and a Super-X divertor. A summary and conclusions are presented in section 5.

## 2. Experimental setup and diagnostics coverage

This study has been performed on the Tokamak à Configuration Variable (TCV) [25] (major radius  $R_0 = 0.88 \text{ m}$ , minor radius  $a = 0.24 \text{ m}$ ,  $B_0 \approx 1.44 \text{ T}$ ). Figure 1 plots typical DN configurations developed and studied in this work. For the discharge presented in the left panel, the High-Field Side baffle, introduced in the framework of the TCV Divertor Upgrade [26, 27], was installed, while the longer Low-Field Side baffle was absent. In the DN configuration, with this inner baffle, the particle flux reaching the top of the baffle is lower by 1-2 orders of magnitude than that reaching the (lower) inner strike point. Therefore, this baffle is not expected to affect significantly the measurements. The radial position of the gas valve used for the fueling is indicated by the black rectangle in the left panel of figure 1.  $D_2$  is injected at a

fueling rate controlled by a feedback loop based on the line-averaged density  $\langle n_e \rangle$  measured by a vertical chord of a Far-Infrared interferometer. Wall-embedded Langmuir Probes (LPs) [28, 29, 30] are indicated by the blue dots with red squares indicating the locations of the Thomson Scattering measurements [31]. Two fast infrared cameras are used to simultaneously measure the divertor heat loads at both lower strike points [32]. Their fields of view are indicated by the cyan areas drawn in figure 1. The MANTIS diagnostic [33, 34] (not shown) images the lower divertor simultaneously at several wavelengths. In this paper, we will focus upon CIII (465.8 nm) line emission. The captured images are tomographically inverted to obtain two-dimensional poloidal maps of the emissivity. It was shown in previous TCV studies that the position of the CIII front along a divertor leg provides a convenient tool to assess the detached status of the divertor [35, 10, 36]. This front is determined as the location where the emissivity profile along the outer leg has decreased by 50% [35]. Due to its strong dependency upon the local electron temperature, the CIII front location was found to be a good indicator of a low temperature region along the outer leg. The upper divertor is also imaged using a fast camera (FastCam) equipped with a similar filter to monitor the same CIII emission line. However, this system's alignment was not calibrated, impeding tomographic inversions. Therefore, the location of the CIII front along the upper divertor leg is estimated from toroidally integrated measurements, as described in section 4.2.

### 3. Double-null balance investigation

In a reactor, operation in a magnetically balanced DN divertor will be challenging, and the precision required for the magnetic balance of the configuration may place significant constraints on the control system, equilibrium diagnostics and reconstruction capabilities. Therefore, it is critical to know how quantities of interest, such as the power sharing between the targets, are affected by the magnetic balance.

The magnetic balance is quantified by  $\delta R_{sep}$ , the radial distance between the two separatrices at the outer midplane, estimated here from the magnetic equilibrium reconstruction code LIUQE [37]. In our convention,  $\delta R_{sep} < 0$  mm corresponds to an Upper Single Null (USN) while  $\delta R_{sep} > 0$  mm corresponds to a Lower Single Null (LSN). A magnetically balanced DN is achieved when  $\delta R_{sep} = 0$  mm. In this section, we discuss a set of constant line-averaged density discharges where  $\delta R_{sep}$  is varied from  $-32$  mm to  $16$  mm within a single discharge, Figure 2. Here, parameters ( $I_P = 300$  kA,  $B_t = 1.44$  T,  $\langle n_e \rangle = 6.8 - 8 \times$

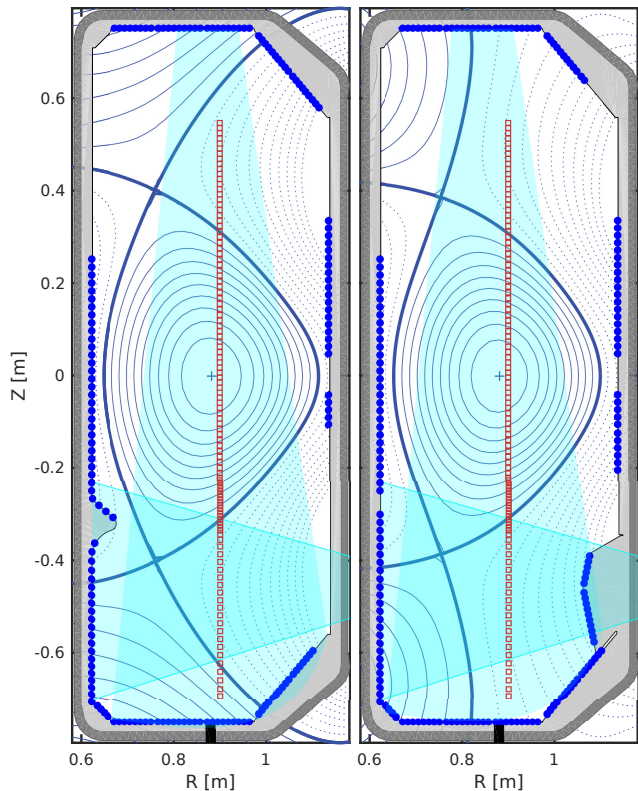


**Figure 1.** Typical DN shapes investigated in this paper. The blue dots correspond to wall-embedded Langmuir probes that were available for all shots presented in this study. The red squares indicate the locations of the Thomson Scattering measurements. The two cyan regions show the field of view of the two infrared cameras. The black rectangle at the bottom of the machine indicates the poloidal location of the gas valve used for fueling.

$10^{19} \text{ m}^{-3}$ ) are kept relatively constant. We note that at this plasma current, the quoted values of line-averaged density result in attached divertor conditions.

Infra-Red measurements show that no power arrives at the lower divertor for  $\delta R_{sep} \ll 0$  mm (Figure 3, panel a). As  $\delta R_{sep}$  is increased, the lower divertor receives an increasing fraction of the exhaust power that saturates as the configuration becomes a LSN. Ultimately, approximately 75% of the power expected from power balance reaches the divertor. This incomplete power balance is a common issue in tokamak plasma research, and the reason for this discrepancy in TCV is currently unknown, but the subject of continued investigation.

The distribution of the power to the lower divertor between outer (blue points) and inner (red points) leg reveals that the outer strike point activates first when transiting to a LSN (Figure 3b). The integrated infrared measurements are well fitted using a logistic fit (equation 1) following analytical considerations for the power sharing between the two outer legs (Figure

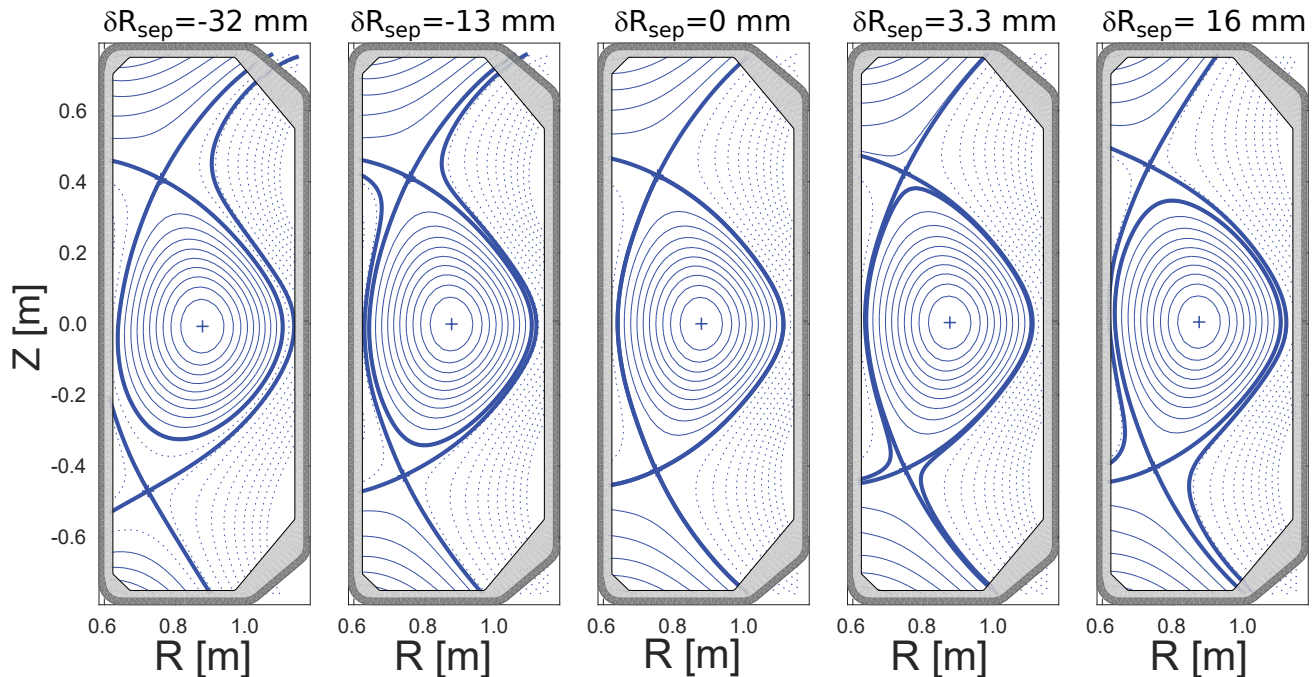


**Figure 2.** The different magnetic configurations achieved during a single discharge where  $\delta R_{sep}$  is varied from  $-32$  mm up to  $16$  mm. The discharge starts from an USN shape (left) and evolves towards a LSN (right), passing by the DN shape (center).

3) [19].

$$P = \frac{P_0}{1 + e^{-\frac{\delta R_{sep} - \delta_0}{\lambda_0}}} \quad (1)$$

This function describes an increase in the power to the strikepoint(s) from 0 to  $P_0$  as  $\delta R_{sep}$  increases from strongly negative to strongly positive.  $\delta_0$  is the value for  $\delta R_{sep}$  at which half of the power increase is achieved.  $\lambda_0$  indicates the sensitivity of  $P$  on  $\delta R_{sep}$  and, within the simplified assumptions of this model [19], is expected to equal the e-folding width of the heat flux,  $\lambda_q$ . When fitting equation 1 to the total power to the lower divertor (the sum of the power to the OSP and to the ISP), figure 3a,  $\lambda_0$  ( $\lambda_0 \approx 3$  mm) is indeed of the order of the  $\lambda_q$  estimated from target IR measurements ( $\lambda_q \approx 3 - 4$  mm, typical for such plasma current in L-Mode). According to equation 1, for  $|\delta R_{sep}| \lesssim \lambda_q/2$  (assuming  $\delta_0 \approx 0$ ) a good power sharing between upper and lower divertor can be achieved, with between 37% to 63% of the exhaust power going to the lower one.

Considering now the power to the inner and outer lower strike-points separately, Fig. 3b, we find that, for  $|\delta R_{sep}| < 5$  mm, between 55% and 75% of the power going to the lower divertor arrives at the lower outer strike-point. A significant fraction of the exhaust power directed to the lower divertor is, thus, still transported to the lower inner target (between 25%-45%, and around 30% for  $\delta R_{sep} = 0$  mm). This fraction is higher than that for L-modes in Alcator C-Mod [19] and that expected from first principle

simulations [38]. Exploring further this difference would require simultaneous IR diagnosis of all four strike-points of these configurations, currently not available. While ballooning transport favors energy exhaust at the Low-Field Side, a fraction of the energy may still be exhausted at the High-Field Side, reaching the inner targets. Another possible reason for this high level of power to the inner strike-point could be due to the presence of transport in the vicinity of the X-points (both at the top and the bottom, due to  $E \times B$  drifts, turbulence,...), that would allow part of the power exhausted through the Low-Field Side to cross the separatrix at the X-point and flow to the inner targets.

Let us now turn to the scrape-off layer width,  $\lambda_q$ . Figure 4 plots  $\lambda_q$  estimates for two values of  $\langle n_e \rangle$  ( $6.8 \times 10^{19} \text{ m}^{-3}$  and  $8 \times 10^{19} \text{ m}^{-3}$ ), the former corresponding to an attached plasma while the latter is slightly detached, as will be shown later in this work. For  $\delta R_{sep} \geq 0$  mm, the lower outer target heat flux profiles, observed with the infrared system, are remapped by projecting the heat flux profile from the divertor to the midplane, and then an Eich-fit is applied to determine  $\lambda_q$  [1].  $\lambda_q$  remains fairly constant ( $\lambda_q \approx 3 - 4$  mm) for all  $\delta R_{sep} > 0$  mm (Figure 4b). In particular, the somewhat complex evolution of  $\lambda_q$  observed in Ref. [20] near  $\delta R_{sep} = 0$  mm is not retrieved, although we are limited by the Infrared coverage that provides no data for  $\delta R_{sep} \leq 0$  mm. This was circumvented by re-evaluating  $\lambda_q$  using Thomson

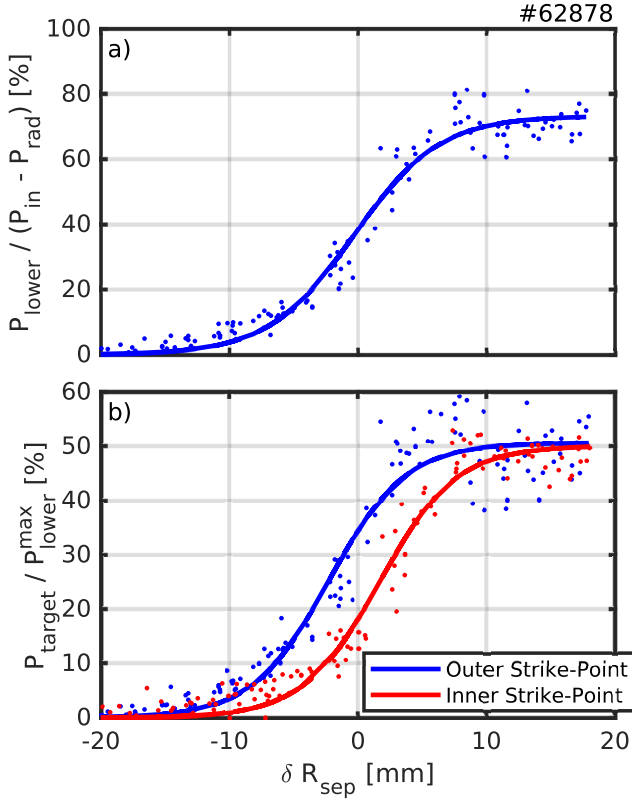


**Figure 3.** (Panel a) Evolution of the normalized total power (inner and outer strike point) going to the lower divertor  $P_{lower}$ , as a function of  $\delta R_{sep}$ , determined from Infrared measurements. (Panel b) Evolution of the power going to the lower outer (blue) and lower inner (red) strike-points, normalized to the maximum power reaching the entire lower divertor when  $\delta R_{sep} \gg 0$ , as a function of  $\delta R_{sep}$ . The solid lines correspond to logistic fits, eq. 1.

Scattering (TS) measurements of  $\lambda_{T_e}$  and  $\lambda_n$ , the characteristic decay length of the electron temperature and density, following the procedure detailed in Ref. [39].  $\lambda_q$  can be estimated from

$$\lambda_q^{cond} = \frac{2}{7} \lambda_{T_e} \quad (2)$$

for a conduction-limited SOL, and

$$\lambda_q^{conv} = \left( \frac{3}{2\lambda_{T_e}} + \frac{1}{\lambda_n} \right)^{-1} \quad (3)$$

for a flux-limited SOL. Although  $\lambda_q$  differs substantially when evaluated from equation 2 or 3, it remains fairly constant with  $\delta R_{sep}$ , figure 4a.

Ultimately, a key quantity of interest is the peak heat flux. Its value at the lower outer target decreases as the configuration evolves towards an USN (Figure 4c). Near  $\delta R_{sep} = 0$  mm, it is 60% of its value in LSN, showing that DN remains a promising solution to reduce the target peak heat flux.

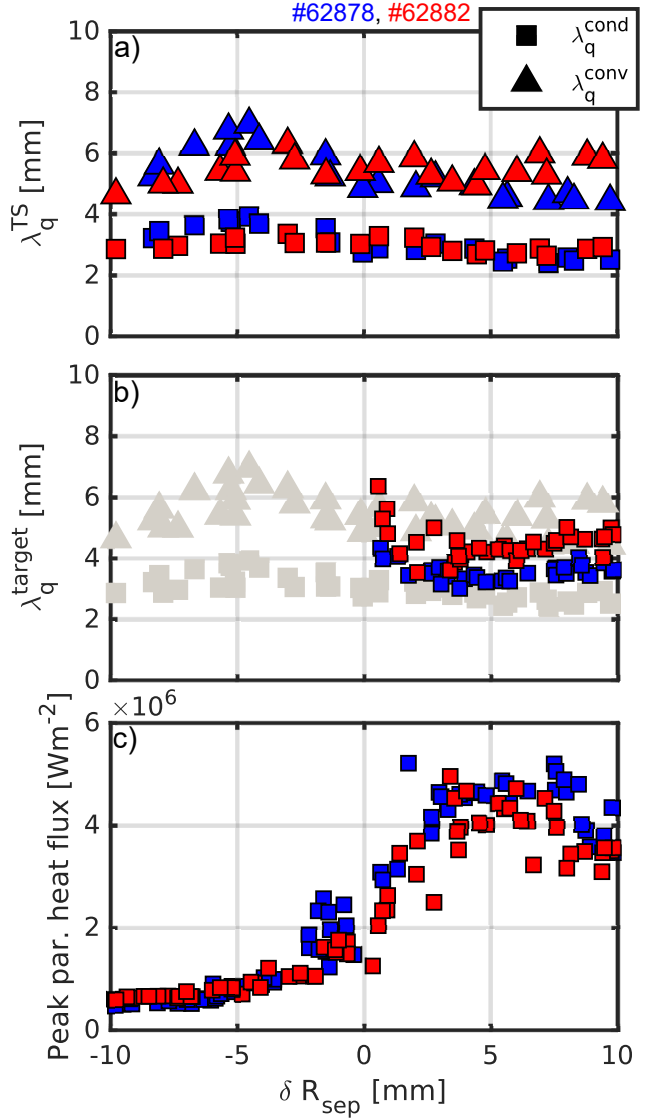


**Figure 4.** (panel a) Upstream  $\lambda_q$  determined from Thomson Scattering measurements using equations 2 and 3 [39] as function of  $\delta R_{sep}$ . (panel b) Lower outer target  $\lambda_q$  (remapped upstream) determined from Infrared measurements as function of  $\delta R_{sep}$ . The grey data points correspond to the points of panel (a). (panel c) Peak parallel heat-flux determined from Infrared measurements as function of  $\delta R_{sep}$  at the lower outer target. Blue and red datapoints correspond to a discharge at  $\langle n_e \rangle = 6.8 \times 10^{19} \text{ m}^{-3}$  and  $\langle n_e \rangle = 8 \times 10^{19} \text{ m}^{-3}$ , respectively.

## 4. Investigation of detachment in double-null configurations

### 4.1. Motivation for alternative divertor geometries and their implementation as DNs

We commence this section with a short summary of the potential benefits that may be expected from alternative divertor magnetic geometries in terms of detachment behavior. For a more detailed analysis, the reader is referred to Ref. [40, 10] and references therein.

Using an extended two-point model that includes the variations of the major radius along the divertor leg and radiation losses, the target electron temperature  $T_e^t$  is found to scale as [10]

$$T_e^t \propto \frac{(q_{\parallel}^u)^{10/7} (1 - f_{rad})^2 R_u^2}{n_u^2 L_{\parallel}^{4/7} R_t^2} \quad (4)$$

where  $q_{\parallel}^u$  is the upstream parallel heat flux,  $n_u$  the upstream density,  $f_{rad}$  the fraction of  $q_{\parallel}^u$  that is radiated before reaching the target,  $L_{\parallel}$  the parallel connection length,  $R_u$  the upstream radial position and  $R_t$  the target radial position. Equation 4 implies that low  $T_e^t$  can be achieved for a given  $q_{\parallel}^u$  and  $n_u$  by increasing  $f_{rad}$ ,  $L_{\parallel}$ , or  $R_t$ . Here, we focus mainly on  $L_{\parallel}$  and  $R_t$ , which are related to the divertor geometry.  $L_{\parallel}$  can be increased, for instance, by increasing the poloidal flux expansion ( $f_x$ ), which also leads to an increase of the divertor volume, possibly leading to an increased  $f_{rad}$ . In TCV L-mode plasmas, while increasing  $f_x$  leads to deeper detachment, for a given line-averaged density, a strong effect on the detachment threshold is not observed [10]. Increasing the radial position of the strike-point,  $R_t$ , results in the so-called Super-X configuration. However, TCV experiments found little influence on detachment characteristics in non-baffled conditions [10], a result recovered for intermediate  $R_t$  cases in SOLPS-ITER simulation [41] and explained by a reduction in divertor neutral trapping with increasing  $R_t$ .

One hypothesis that is often used when predicting the behavior of advanced divertor geometries is that  $q_{\parallel}^u$  remains constant for all geometries. In general however, alternative geometries only affect one (typically the outer) divertor leg. The power flux leaving the separatrix from the low-field-side will be distributed between the two main divertor legs. Assuming that this power is transferred to the divertor targets via conduction (as assumed by the two-point model), that the upstream temperature is considerably higher than the target temperature, that  $B \propto 1/R$  and that no dissipation occurs along the flux tube, one can show that [42]

$$\frac{q_{\parallel}^o}{q_{\parallel}^i + q_{\parallel}^o} = \frac{1}{1 + \frac{\mathcal{L}_{\parallel}^o}{\mathcal{L}_{\parallel}^i}} \approx \frac{\mathcal{L}_{\parallel}^i}{\mathcal{L}_{\parallel}^o} \quad \text{for } \mathcal{L}_{\parallel}^o \gg \mathcal{L}_{\parallel}^i \quad (5)$$

where  $q_{\parallel}^o$  (resp.  $q_{\parallel}^i$ ) is the parallel heat flux to the outer (resp. inner) target and  $\mathcal{L}_{\parallel}^o$  (resp.  $\mathcal{L}_{\parallel}^i$ ) is the parallel connection length to the outer (resp. inner) target weighted by the inverse major radius [42]. Alternative geometries, such as the X-Divertor, will tend to increase  $\mathcal{L}_{\parallel}^o$ . However, according to equation 5, this also results in a reduction in  $\frac{q_{\parallel}^o}{q_{\parallel}^i + q_{\parallel}^o}$ , and, thus, an increase in the power to the inner target. Such a change

in power sharing with connection length was shown experimentally in Ref. [42]. Optimizing the geometry at the outer target for detachment may, therefore, come at the expense of the inner target, where applying alternative geometries is more challenging [6]. A possible solution is the DN configuration. By distributing most of the output power between two outer targets, the power sharing issue between inner and outer legs is naturally addressed. Furthermore, alternative geometries may more easily be applied to the two main active legs in the DN, being both outer legs. Therefore, in the following, we extend the alternative geometries studies in TCV to poloidal flux expansion in DN and DN Super-X configurations.

#### 4.2. DN vs LSN for different values of poloidal flux expansion

We investigate the impact of poloidal flux expansion on detachment in LSN and DN. The scenario is an Ohmically heated plasma with a plasma current of  $I_p = 250$  kA and with the ion  $\nabla B$ -drift pointing upwards in the TCV chamber. The divertor shape is varied to change  $f_x$  at the target (figure 5a-c). The line-averaged density  $\langle n_e \rangle$  is linearly increased from  $5 \times 10^{19} \text{ m}^{-3}$  to  $11 - 12 \times 10^{19} \text{ m}^{-3}$  in the LSN configurations, whereas the DN configurations generally disrupt at lower densities ( $10 \times 10^{19} \text{ m}^{-3}$ ). For the Double-Nulls,  $\delta R_{sep}$  typically stays within within -1mm and +2mm, that is, below the estimated  $\lambda_q$  (4 - 5 mm), Figure 5f. These discharges are summarized in Table 1.

Discharge	$I_p$	target $f_x$	Configuration
66260	250 kA	$\approx 3.5$	DN
66263	250 kA	$\approx 6$	DN
66619	250 kA	$\approx 6 - 8$	DN
66265	250 kA	$\approx 3.5$	LSN
66269	250 kA	$\approx 6$	LSN
66620	250 kA	$\approx 6 - 8$	LSN

**Table 1.** Summary of the main plasma discharges used in this section.

In LSN, power is shared between the inner and outer leg, whereas in DN, the power is mainly shared between upper and lower outer legs. In the following, we therefore compare the lower outer DN leg with the lower LSN outer leg and the DN's upper outer leg with the LSN's inner leg.

We first consider the lower outer divertor of the DN and the outer divertor of the LSN. A clear roll-over in the integrated target ion flux is observed at the outer target of the LSN, at  $\langle n_e \rangle \approx 8.5 \times 10^{19} \text{ m}^{-3}$  for  $f_x = 6 - 8$  and  $\langle n_e \rangle \approx 9.5 \times 10^{19} \text{ m}^{-3}$  for  $f_x = 3.5$ , Figure 6c. In the DN configurations, a saturation (for  $f_x = 3.5$  and  $f_x = 6$ ) of the integrated target ion flux is observed already at  $\langle n_e \rangle \approx 6.5 \times 10^{19} \text{ m}^{-3}$  (Figure

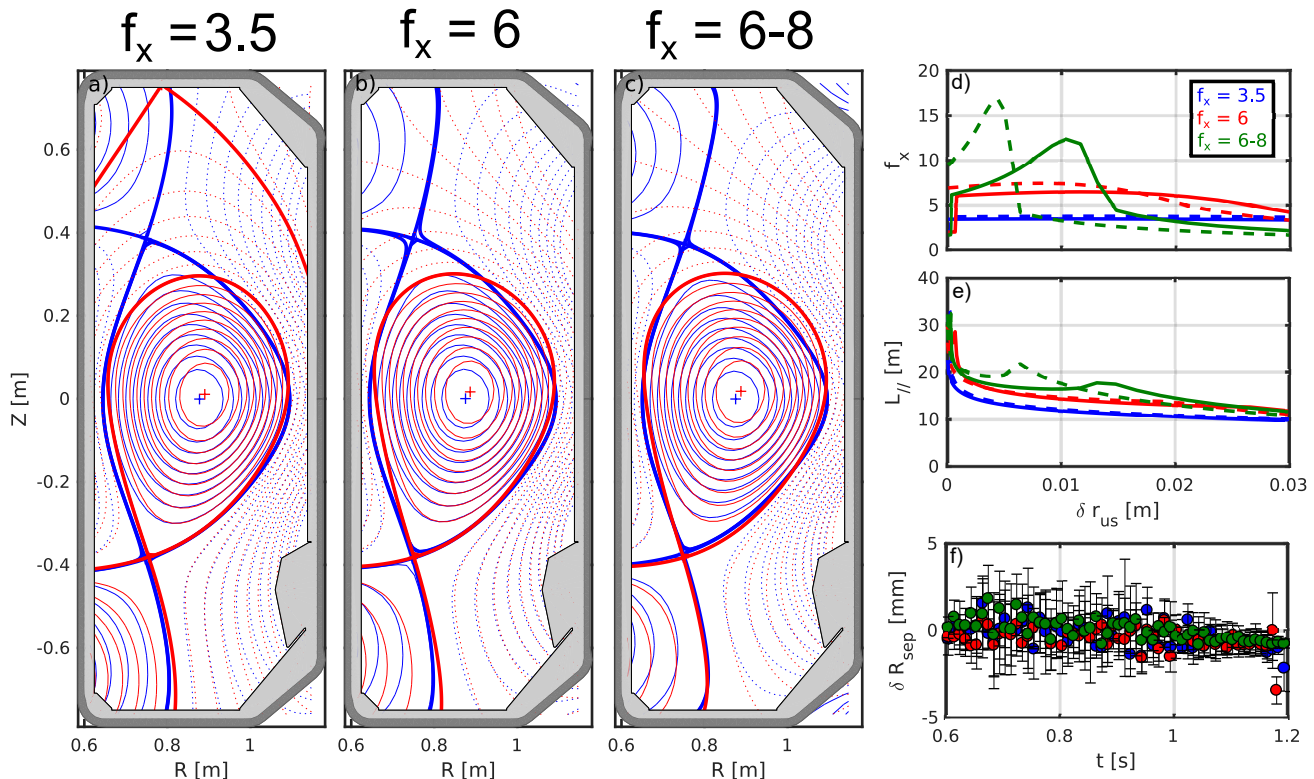


**Figure 5.** Left panels (a,b,c): DN configurations (blue) with varying flux expansion, compared to reference LSN (red). Right panels: d) Outer targets flux expansion of the DN cases, as a function of the distance to the separatrix (remapped upstream). e) Parallel connection length  $L_{\parallel}$  to the outer targets, as a function of the distance to the separatrix (remapped upstream). The solid (resp. dashed) lines indicate quantities at the lower (resp. upper) outer target. f)  $\delta R_{sep}$  inferred from the equilibrium magnetic reconstruction as a function of time.

6c), where the peak ion flux is also seen to roll-over (Figure 6d) for  $f_x = 3.5$ .

The earlier, LP-inferred, detachment of the lower outer leg in DN is consistent with the CIII emissivity front observations, that show an earlier movement of the CIII front for the DN, another indication of a lower detachment threshold (Figure 7). Defining a detachment threshold of the lower outer leg, somewhat arbitrary, as a poloidal distance of 15 cm between the CIII front and the X-point [43, 36], we obtain a threshold at  $\langle n_e \rangle = 6.5 \times 10^{19} \pm 10\% \text{ m}^{-3}$  for the DN and  $\langle n_e \rangle = 8.7 \times 10^{19} \pm 10\% \text{ m}^{-3}$  for the LSN configurations. This is compatible with the observations from the target current measurements in Figures 6c and 6d.

Overall, these discharges show no clear dependence on  $f_x$  in terms of detachment onset. For the LSN, both integrated target ion flux and CIII front displacement show a similar, non-monotonic trend with  $f_x$ , that is however small enough to possibly stem from experimental scatter. For the DN, the CIII front movement at  $f_x = 3.5$  and  $f_x = 6$  are almost identical. At  $f_x = 6 - 8$ , the front moves even later. However, this effect is relatively small and might also be related to a slightly larger  $\delta R_{sep}$  in this case (Figure 5f) or to

experimental uncertainties.

We now compare the upper outer leg of the DN to the inner leg of the LSN. In DNs, the integrated particle flux continues to increase with  $\langle n_e \rangle$  (Figure 6a), while a decrease in the peak parallel particle flux can be observed (Figure 6b) at  $\langle n_e \rangle \approx 7.5 \times 10^{19} \text{ m}^{-3}$ . Thus, the upper outer leg starts to (partially) detach immediately before the disruption. In LSN, there are also indications of a saturation of the integrated particle flux, associated with a decrease of the peak parallel particle flux. This decrease occurs at higher density than in the DN and at a similar density as the roll-over of the LSN's outer leg. This could indicate that the inner strike point in the LSN cases is starting to partially detach just before the disruption of the LSN.

CIII filtered images were used to further compare the dynamics of the upper strikepoint of the DNs to the inner strike point of the LSN. In DN, we observe a movement of the CIII emission front towards the upper X-point for all cases (Figures 8 and 9). The fastCam diagnostic was not adequately spatially calibrated to permit an estimate of the CIII front movement from a tomographically inverted emissivity map as in Figure 7. Simpler image processing was instead used to assess

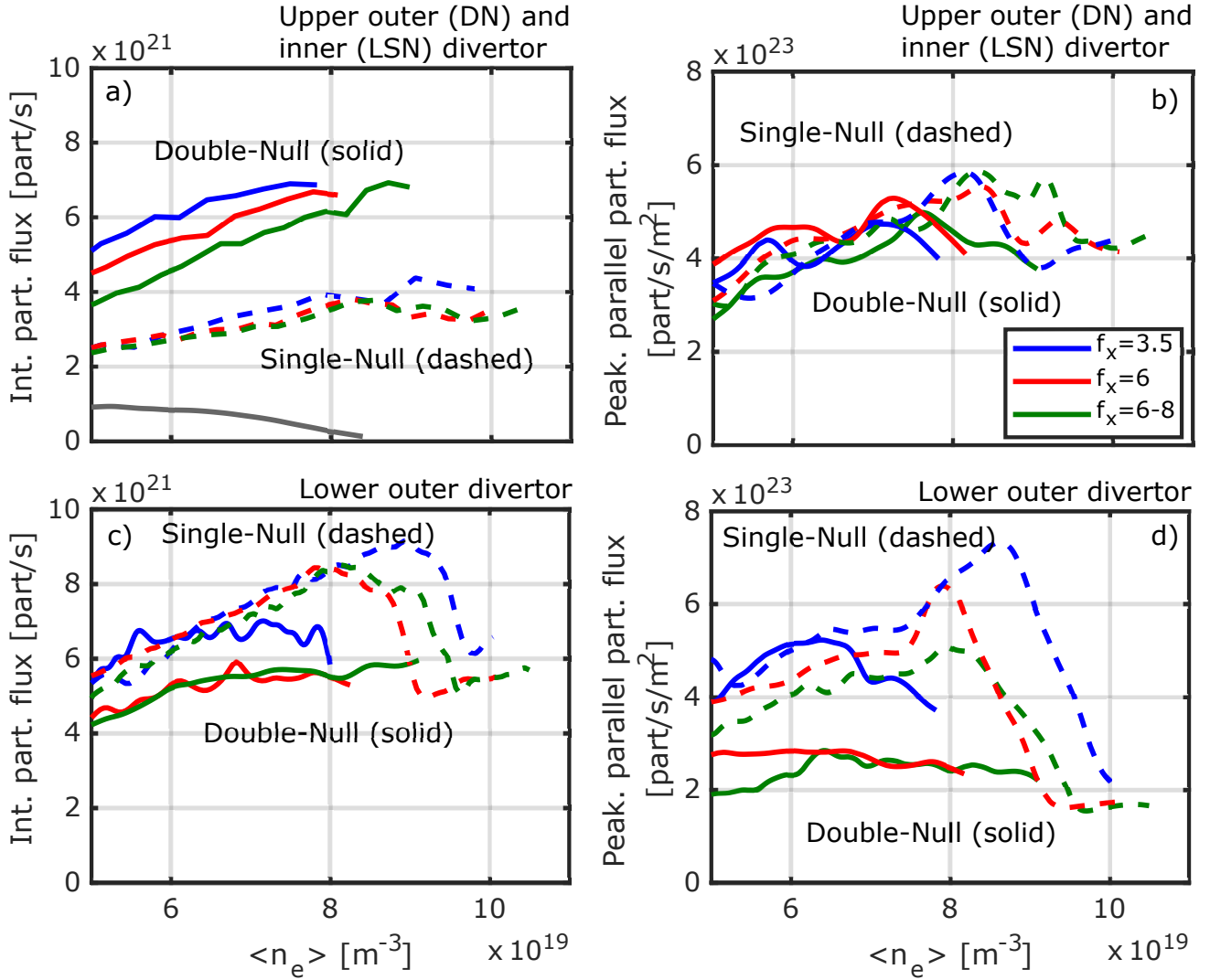


**Figure 6.** (panel a) Integrated particle flux going to the upper outer leg of the DN and the inner leg of LSN configurations for varying flux expansion, as a function of  $\langle n_e \rangle$ . The grey line, plotted for reference, corresponds to the ion flux going to the lower inner leg of the  $f_x = 3.5$  DN case. (panel b) Peak parallel particle flux going to the upper outer leg of the DN and the lower inner leg of the SN, as a function of  $\langle n_e \rangle$ . (panel c and d) Integrated and peak particle flux going to the lower outer leg of the DN and LSN configurations for varying flux expansion, as a function of  $\langle n_e \rangle$ .

the CIII front position from the toroidally integrated images. A distance along the leg is computed by determining the number of pixels between the X-point and the CIII front normalized to the number of pixels between the X-point and the outer strike-point, in the vertical direction. To reduce noise, a Gaussian Smoothing Filter with  $\sigma = 2$  is applied to the image frames before the CIII front position determination. This is then applied to the images of the upper divertor and, for comparison, to the lower divertor images (Figure 9). For the lower divertor, this yields similar results to the MANTIS inversions (Figure 7). For the upper divertor, the CIII front is found to move slightly earlier than for the lower leg of the LSN, in agreement with Langmuir Probe measurements. The movement

appears rapid and precedes a disruption, indicating a narrow detachment window in  $\langle n_e \rangle$  for the upper outer divertor leg of the DN. For LSN, a movement of the CIII front, along the inner leg, towards the X-point is also observed, figure 10. This indicates inner leg cooling, although it occurs when  $\langle n_e \rangle$  is similar or higher to that at which the CIII front recedes from the outer target, in agreement with LP observations (Figure 6).

The LP measurements and CIII front analysis in figures 6-10 thus suggest the following order in detachment onset as a function of  $\langle n_e \rangle$  for the active legs in LSN and DN. First, in these discharges with the ion  $\nabla B$ -drift pointing upwards, the lower outer leg of the DN detaches. Next, it is the upper outer leg

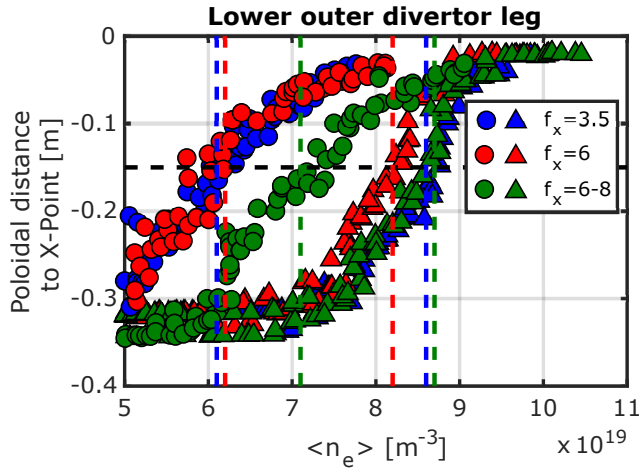


**Figure 7.** Poloidal distance between the CIII front and the X-point as a function of the line-averaged density  $\langle n_e \rangle$  for the lower outer divertor leg of the DN (circles) and the SN (triangles), determined from tomographic inversions.

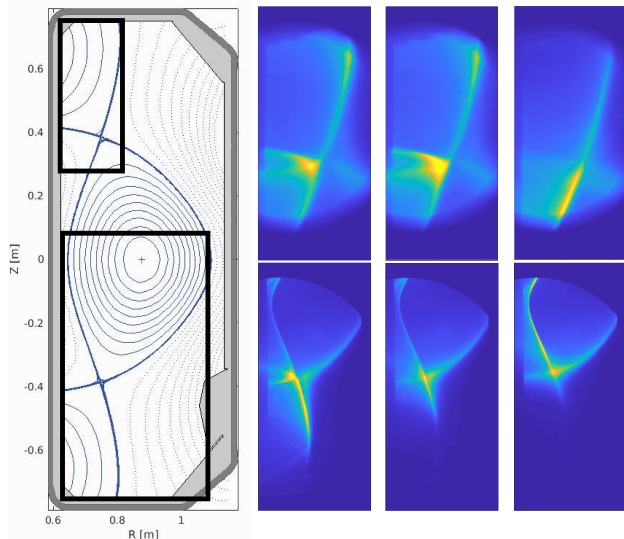


**Figure 8.** Left panel: magnetic geometry of the  $f_x = 3.5$  case. The black rectangles indicate the approximate Field of View of the FastCam imaging the upper divertor (top rectangle) and of the MANTIS diagnostic (lower rectangle). Right panels: Spectrally filtered (CIII) images of the upper divertor (top line) and bottom divertor (bottom line) at different  $\langle n_e \rangle$  for the  $f_x = 3.5$  case investigated in this section.

of the DN that detaches. It does so relatively quickly, preceding a disruption. Only later, the outer leg of the LSN and then the inner leg of the LSN detach. In the following, we demonstrate, more directly, that in a DN, the CIII fronts of the two active legs can be closer to the X-points than the CIII front in both active legs of a comparable SN. We perform a  $\delta R_{sep}$  scan, similar to the higher current case in 2, for  $f_x = 3.5$  ( $I_P = 250$  kA). The target line-averaged density is  $\langle n_e \rangle \approx 7.4 \times 10^{19} \text{ m}^{-3}$ , where we expect the DN's CIII front to be detached. With continual shape changes,

density control was imperfect with  $\langle n_e \rangle$  changing  $\pm 10\%$  around the nominal value, as shown in the inset of figure 11. The lower divertor's CIII front location reveals that in the LSN phase, the fronts of both inner and outer legs remain at the target, indicating that the plasma remains attached. As the configuration shifts towards a DN, the front of the lower outer leg moves up, indicating a progressive lowering of the outer leg temperature (Figure 11). In the DN phase, the CIII fronts in both active legs are clearly separated from the targets. We note, however, that the CIII front is closer to the target for the upper divertor, in agreement with the observations of figure 9, and may be a manifestation of the effect of drifts. As the shape transitions from DN to USN, the CIII front moves towards the outer upper target along the outer leg and also re-attaches to the inner target.

We thus find that the DN shows an easier access to detachment, for both its active legs, than the SN. Furthermore, the change from SN to DN clearly has a much stronger effect than the two-fold increase in poloidal flux expansion explored in both geometries. In Fig. 12, we present the change with geometry of another important quantity, the total radiated power,  $P_{rad}$ , estimated from bolometry. DN plasmas radiate a higher absolute power (Figure 12a) and a higher normalized power (normalized to the Ohmic heating power) for a given  $\langle n_e \rangle$  (Figure 12b). With four strike points, this may be explained by a change in carbon transport, or increased carbon erosion, leading to higher impurity concentration and, consequently, higher levels of radiation.  $Z_{eff}$  and the core radiation of LSN and DN cases do not, however, show significant differences. This indicates that the improved radiation fractions stem from the activity surrounding two divertors and two active X-points in the DN configuration, and the presence of two radiation fronts, increasing the potential interest of DN configurations as more efficient radiators. In the LSN, the low  $f_x$  case appears to radiate slightly less power than higher  $f_x$  cases, perhaps, hinting at some effect of  $f_x$  on power radiation. This contrasts to DN configurations, where the radiated power is very similar for all  $f_x$  (Figure 12).

To conclude this section, it is found that transiting from LSN to DN configurations leads to a decrease in the detachment threshold, together with an increase in the radiated power. It also seems that the earlier detachment is reflected in a lower density limit, where detachment of the upper outer leg only just precedes a disruption. Increasing the flux expansion by a factor 2 at the outer targets does not lead to a significant improvement of the detachment properties of the divertors.

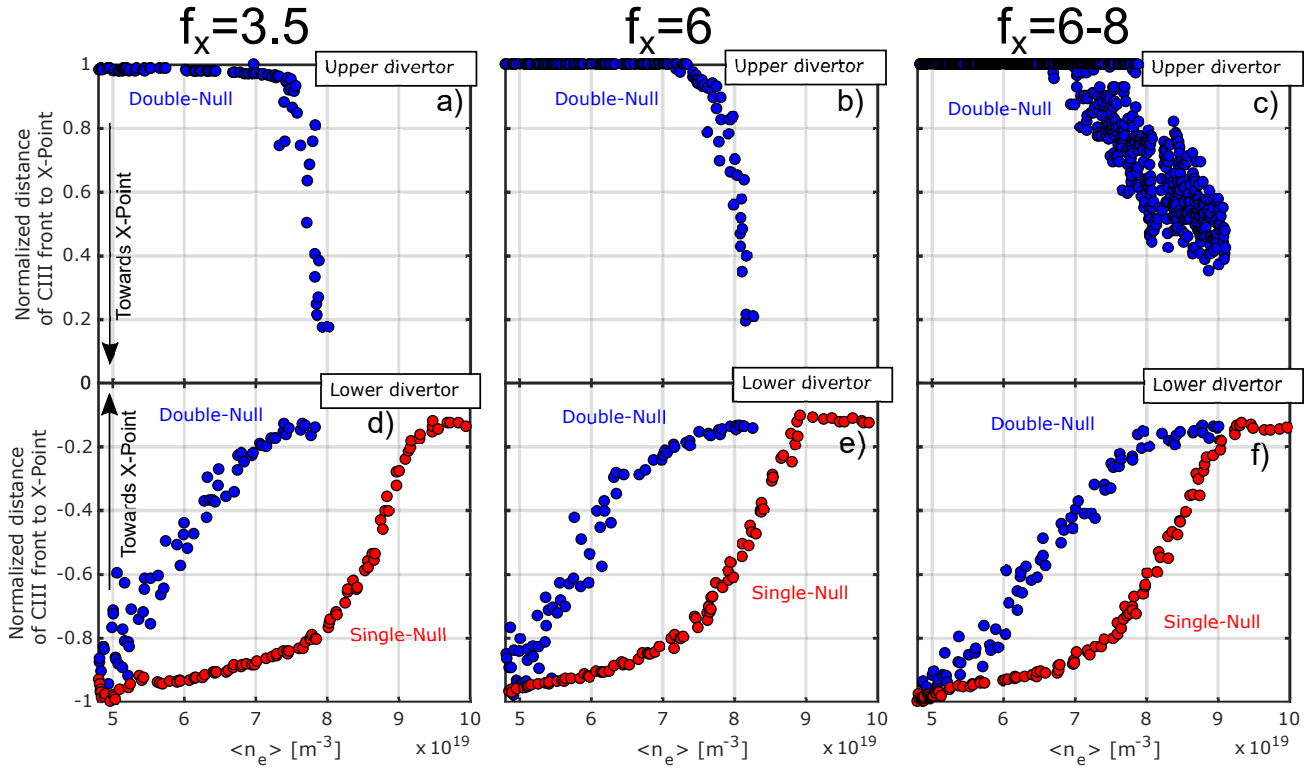


**Figure 9.** (top line) Normalized distance of the CIII front to the X-point in the upper outer leg for the  $f_x = 3.5$  (panel a),  $f_x = 6$  (panel b),  $f_x = 6 - 8$  (panel c) DN cases, as a function of  $\langle n_e \rangle$ . (bottom line) Normalized distance of the CIII front to the X-point in the lower outer leg for the  $f_x = 3.5$  (panel a),  $f_x = 6$  (panel b),  $f_x = 6 - 8$  (panel c) Lower Single Null (red) and DN (blue) cases, as a function of  $\langle n_e \rangle$ . In this figure, a non-tomographic technique is used to determine the CIII front position.

#### 4.3. DN vs LSN for different values of $R_t$

Here, we investigate the impact of the Super-X divertor (total flux expansion) on detachment in LSN and DN. The chosen scenario is an Ohmically heated plasma with a plasma current of  $I_p = 300$  kA with the ion  $\nabla B$ -drift pointing away from the lower X-point. The shape of the divertor is modified to change the target major radius (left panels of figure 13). The line-averaged density  $\langle n_e \rangle$  is then linearly increased from  $5$  to  $10 \times 10^{19} \text{ m}^{-3}$  in the LSN configurations, whereas the DN configurations disrupt at lower densities. For the DNs,  $\delta R_{sep}$  is typically within  $\pm 3$  mm, Figure 13, while the estimated  $\lambda_q$  for these discharges is around 4 mm, Figure 3. These discharges are summarized in Table 2.

Discharge	$I_p$	$R_t$	Configuration
63360, 63366	300 kA	0.99 m	DN
63363	300 kA	0.76 m	DN
63361	300 kA	0.99 m	LSN
63365, 63389	300 kA	0.76 m	LSN

**Table 2.** Summary of the main plasma discharges used in this section.

A rise of the integrated particle flux at the lower

divertor is seen in DN as  $\langle n_e \rangle$  increases, that rolls over at approximately  $\langle n_e \rangle \approx 7.5 \times 10^{19} \text{ m}^{-3}$  for high  $R_t$  and  $\langle n_e \rangle \approx 8.2 \times 10^{19} \text{ m}^{-3}$  for the medium  $R_t$  (Figure 14b). This roll-over occurs at higher  $\langle n_e \rangle$  for the LSN ( $\langle n_e \rangle \approx 9.5 \times 10^{19} \text{ m}^{-3}$  for high  $R_t$  and  $\langle n_e \rangle \approx 11 \times 10^{19} \text{ m}^{-3}$  for medium  $R_t$ ) (Figure 14b). For DN, the flux to the lower divertor appears higher than to the upper divertor (Figure 14a), which is surprising, as one would expect them to be similar or their ratio reversed, since the  $\mathbf{E} \times \mathbf{B}$  is directed upwards. This could, in part, be ascribed to the slight imbalance of the configurations towards LSN, as shown in figure 13. The integrated particle flux to the upper outer divertor in DN saturates at  $\langle n_e \rangle \approx 9 \times 10^{19} \text{ m}^{-3}$  for both  $R_t$ . For LSN, the flux to the inner target continues to increase with  $\langle n_e \rangle$  in both configurations, a sign that the inner leg remains attached.

From Langmuir probe measurements, and consistent with the findings in 4.2, the DN's lower outer leg detaches first, followed shortly by the upper outer leg. The outer leg of the LSN detaches only at values of  $\langle n_e \rangle$  that are similar, or higher, to those at which the upper outer leg detaches in DN. These observations are supported by the CIII filtered images. Tomographic inversions of the lower divertor imaging show DN cases feature an earlier movement of the CIII front than the

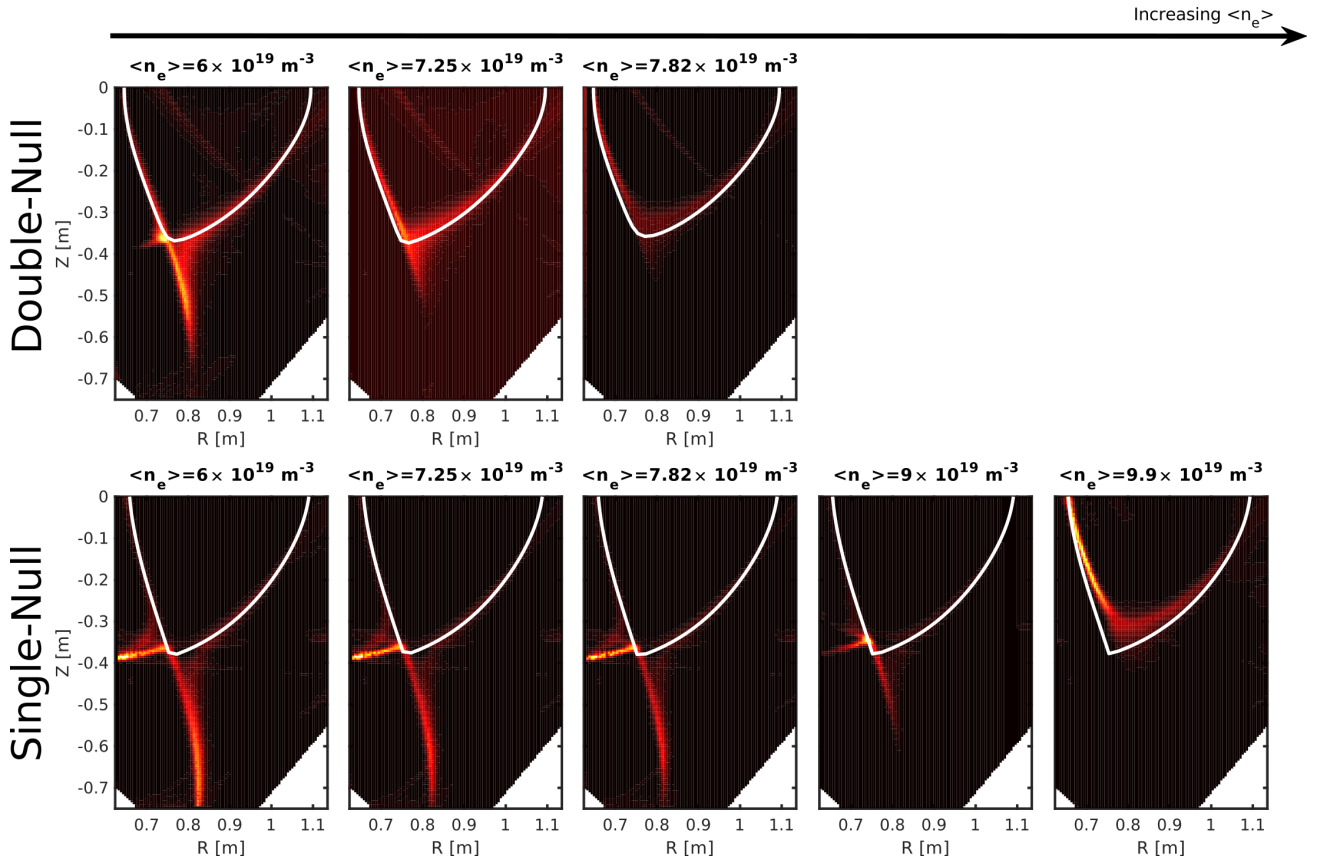


**Figure 10.** Tomographic inversions of the filtered (CIII) images of the lower divertor at different  $\langle n_e \rangle$  for the  $f_x = 3.5$  case investigated in this section in DN (top line) and LSN (bottom line).

LSN, a further indication that they have a lower detachment threshold, Figure 15. As in the previous section, we use a 15 cm X-point radiation front separation to determine the density threshold for detachment onset. For DN, this is  $\langle n_e \rangle \approx 7.25 \times 10^{19} \text{ m}^{-3}$  and  $\langle n_e \rangle \approx 8 \times 10^{19} \text{ m}^{-3}$  for medium and large  $R_t$ , respectively. This 10% difference should not be considered significant, as  $R_t$  changed by 30%, and the result is opposite to the trend expected from equation 4. For LSN, this threshold is  $\langle n_e \rangle \approx 9.5 \times 10^{19} \text{ m}^{-3}$  for both cases.

For the upper divertor, considering toroidal integration effects and a limited field of view that masks part of the leg in the large  $R_t$  case, no direct comparison between the medium and large  $R_t$  may be drawn. In both cases, a clear movement of the CIII front towards the X-point is, however, observed, indicating that the upper leg is also detaching (see Figure 16 for the medium  $R_t$  case.). This is compatible with Langmuir probe data (figure 14), adding further support to detachment in the lower divertor being *not* due to a simple shift of the configuration towards an USN. Thus, similarly to the discharges studies in section 4.2, for an  $\langle n_e \rangle$  ramp, the experimental

sequence becomes: detachment of the lower outer leg, followed by the detachment of the upper outer leg for a DN, and, only at higher values, detachment of the outer leg of the LSN. No clear signs of detachment are apparent here for the LSN's inner leg.

As in the  $f_x$ -scan of section 4.2, the total radiated power,  $P_{rad}$ , estimated from bolometry indicates that DN plasmas radiate more absolute (Figure 17a) and normalized power (wrt Ohmic heating power) for a given  $\langle n_e \rangle$  (Figure 17b) although, at large  $R_t$ , the difference to the LSN reduces for higher  $\langle n_e \rangle$ .

Let us return to the question of the required closeness to a perfect DN. We use the CIII front as an indicator of the detached status of the divertor, as it depends strongly on the local temperature. Figure 18 plots the poloidal distance of the CIII outer lower leg front from the X-point as a function of  $\delta R_{sep}$  for two different values of  $\langle n_e \rangle$ . For  $\delta R_{sep} < 0$  mm, the CIII front moves towards the X-point, as expected, since the lower outer divertor ceases to participate. For  $\delta R_{sep} > 0$  mm, however, it remains close to the target. For both values of  $\langle n_e \rangle$ , the CIII front position as a function of  $\delta R_{sep}$  is well parameterized by equation 1, shown as solid lines in figure 18. For

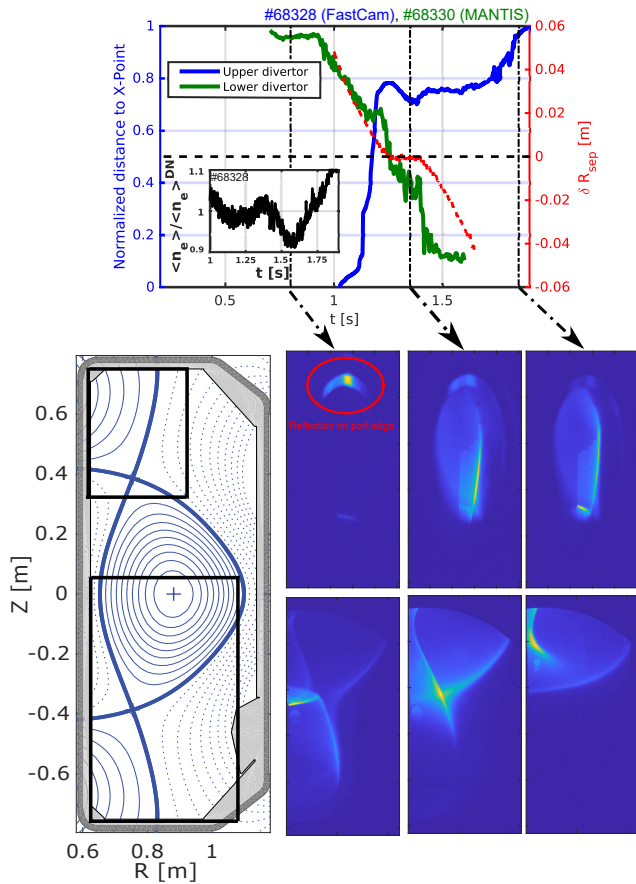


**Figure 11.** (top) (left axis) Evolution of the distance of the CIII front from the X-point for the lower divertor and the upper divertor. (right axis) Evolution of  $\delta R_{sep}$  as a function of time. (insert) Evolution of  $\langle n_e \rangle$  in the discharge, normalized to the average density in the DN phase ( $\langle n_e \rangle = 7.4 \times 10^{19} \text{ m}^{-3}$ ). The vertical dot-dashed lines indicate the times at which the picture displayed in the bottom part of the figure are taken. (bottom) (left) Plasma geometry in the DN phase and fields of view of the FastCam (upper divertor) and MANTIS (bottom divertor). (right, upper row) Images of the upper divertor. (right, lower row) Images of the lower divertor. In shot 68328, no MANTIS data was available. Therefore, Mantis data was taken from a similar discharge (68330).

the lower density case ( $\langle n_e \rangle = 6.8 \times 10^{19} \text{ m}^{-3}$ ), a fit gives  $\lambda_0 \approx 1.6 \text{ mm}$ , i.e. about half of the estimated  $\lambda_q$  for these plasmas. At slightly higher density ( $\langle n_e \rangle = 8 \times 10^{19} \text{ m}^{-3}$ ),  $\lambda_0 \approx 2.9 \text{ mm}$ . This indicates that, as density increases and the divertor plasma approaches detachment, the CIII front location (and hence the outer leg's temperature profile) is less sensitive to changes in  $\delta R_{sep}$ . This may result from a broadening of SOL profiles, observed in TCV in detached conditions for the LSN [44], and that would diminish the required control of the magnetic configuration mentioned in the introduction, in the framework of a reactor operating with a highly dissipative divertor.

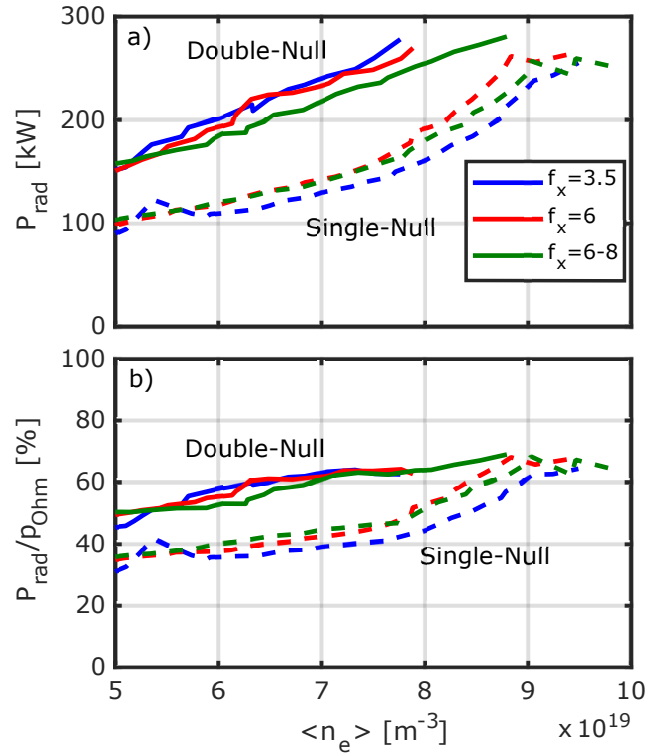


**Figure 12.** Total radiated power  $P_{rad}$  (top panel) and normalized radiated power (lower panel) for LSN (dashed lines) and DN (solid lines) configurations at different flux expansion  $f_x$ .

## 5. Discussion and conclusion

In this article, we explored Double-Null configurations in conventional and advanced geometries, and compared their behavior to Single-Null configurations, with particular emphasis on their detachment characteristics. Results for attached conditions are mostly in line with previous studies on other devices. A high degree of power sharing between upper and lower divertor is achieved for  $|\delta R_{sep}| \lesssim \lambda_q/2$ , resulting in an approximate 30% reduction in the lower outer heat flux (integral and peak) as compared to a Lower Single-Null. Infrared and Thomson-Scattering measurements both indicate no strong dependence of  $\lambda_q$  on  $\delta R_{sep}$ . Langmuir probes and CIII-filtered imaging were used to explore the configurations' detachment characteristics across core density ramps. Transiting from a Single-Null to a Double-Null led to a clear reduction in the detachment threshold (by approx. 20-25%) for the outer targets. The radiated power fraction is also seen to increase by approximately 50%, whereas density limit reduces by  $\sim 10\%$ -20% as compared to LSN counterparts.

One possible limitation of alternative divertor configurations in Single-Null is that an improvement at the outer target potentially comes at the cost of increased problems at the inner target [6]. Such effect is sidestepped by the Double-Null. This

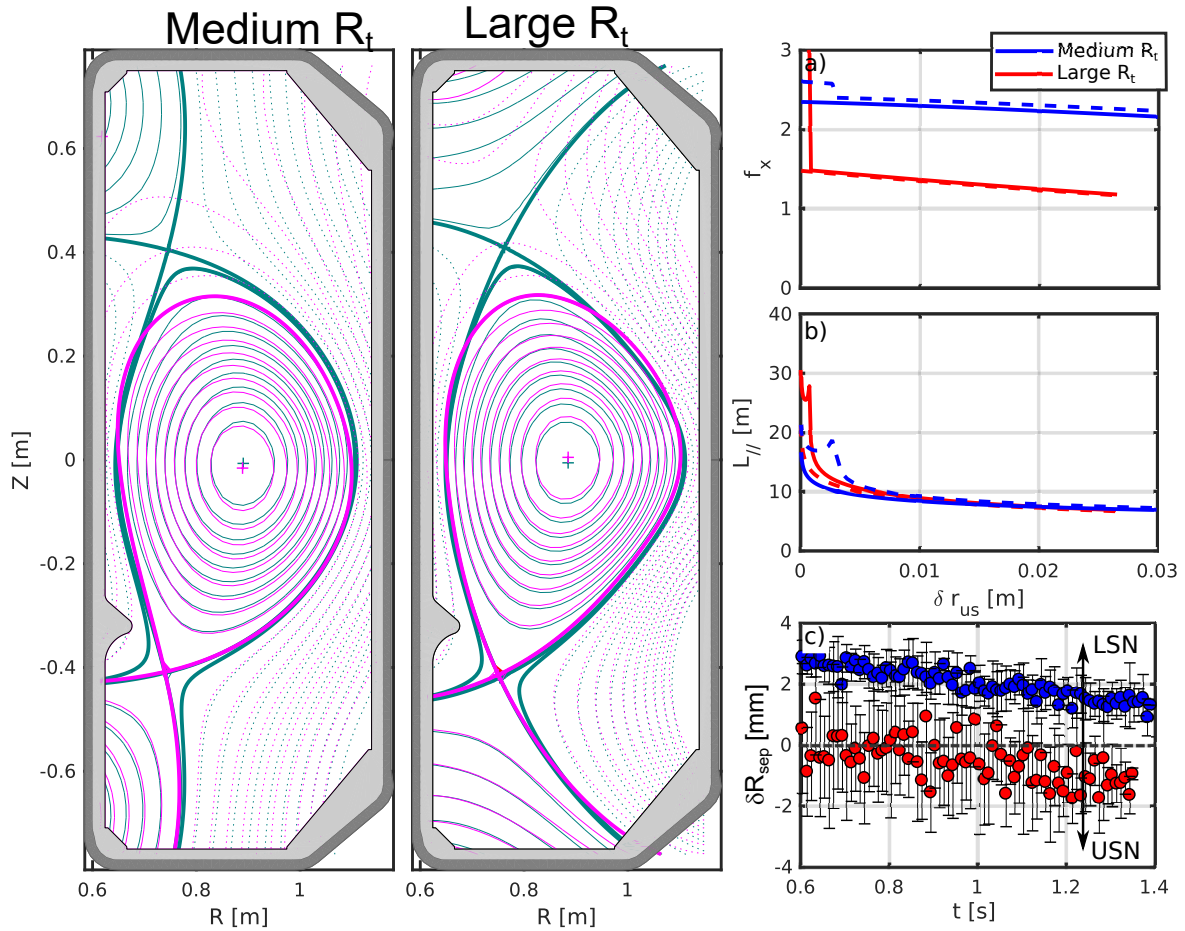


**Figure 13.** Left panels: DN (blue) configurations with varying leg radial positions, compared to reference LSN (magenta). Right panels: a) Outer targets flux expansion of the DN cases, as a function of the distance to the separatrix (remapped upstream). b) Parallel connection length  $L_{||}$  to the outer targets, as a function of the distance to the separatrix (remapped upstream). The solid (resp. dashed) lines correspond to the lower (resp. upper) outer target. c)  $\delta R_{sep}$  inferred from the equilibrium magnetic reconstruction as a function of time

motivated a scan of poloidal flux expansion at both outer strikepoints (by a factor 2), and of the total flux expansion (by 35%). Changing poloidal flux expansion had little effect on the detachment threshold in Single-Null (see also [10]), and no effect for Double-Nulls. Similar observations were drawn for the total flux expansion, where a 30% change in LSN and DN configurations also had little effect on the detachment threshold. This is in line with previous TCV works in LSN geometries where expected effects of poloidal and toroidal flux expansion on the detachment threshold [10, 41] were not recovered. For the ensemble of explored plasma parameters and (relatively modest) geometrical modifications, no strong effects on exhaust performance were observed for Double-Null configurations.

The discharges analyzed in this paper were performed without advanced real-time control of the magnetic balance  $\delta R_{sep}$ . It proved, however, possible to maintain  $\delta R_{sep}$  close to 0 mm. While this could

be more challenging in a bigger machine operating in H-Mode with control coils possibly further away from the plasma, observations on the CIII front behavior indicate that in detached divertors, the margins for control may be higher than in attached divertors.

In conclusion, operation of Double-null with simultaneously detached outer legs shows considerable promise. The expected benefits of alternative divertor configurations, found to be relatively marginal in this study, are expected to be more pronounced for higher power conditions and further optimized configurations, in particular with improved divertor closure [27, 36], which will soon be explored in MAST-U [45]. Finally, we note that this paper investigated the *physics* benefits of operating in a Double-Null configuration, revealing some promising benefits. From an engineering point of view, the suitability of the double-null configuration for reactor operation remains an open question. In particular, maintaining a balanced double-null configuration for a higher power,

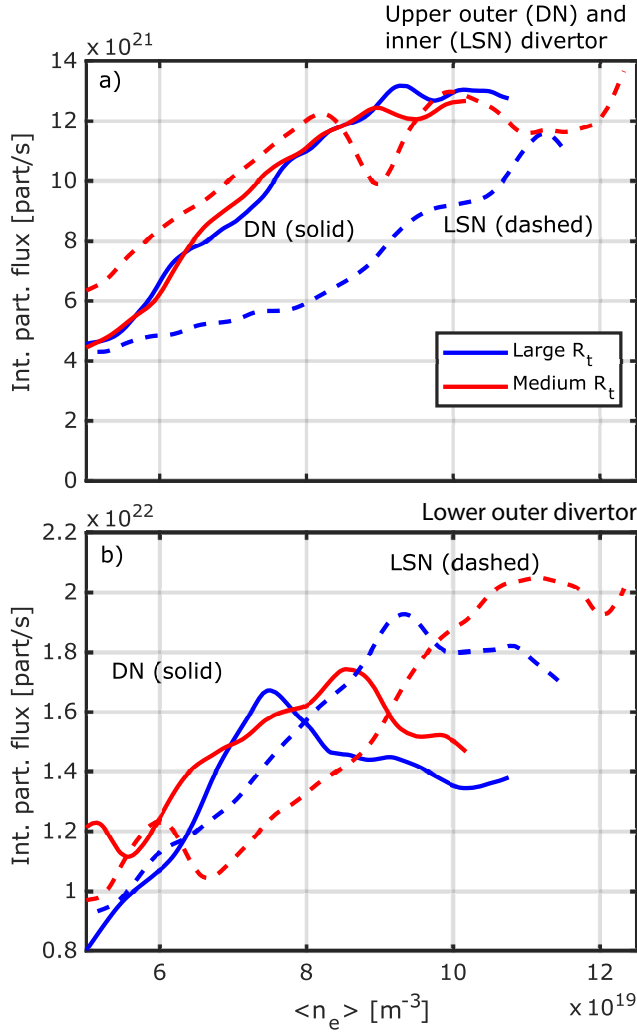


**Figure 14.** (a) Integrated particle flux going to the upper outer leg of the DN configurations and the inner target of the LSN for varying  $R_t$ , as a function of  $\langle n_e \rangle$ . (b) Integrated particle flux going to the lower outer leg of the DN and LSN configurations for varying  $R_t$ , as a function of  $\langle n_e \rangle$ .

higher magnetic field tokamak could prove a very challenging task, due to the expected small value of  $\lambda_q$  [1].

## 6. Acknowledgments

Y. Andrebe is thanked for his assistance in installing the FastCam diagnostic on a TCV upper lateral port. This work was supported in part by the Swiss National Science Foundation. This work has been carried out within the framework of the EUROfusion Consortium and has received funding from the Euratom research and training programme 2014 - 2018 and 2019 - 2020 under grant agreement No 633053. The views and opinions expressed herein do not necessarily reflect those of the European Commission.

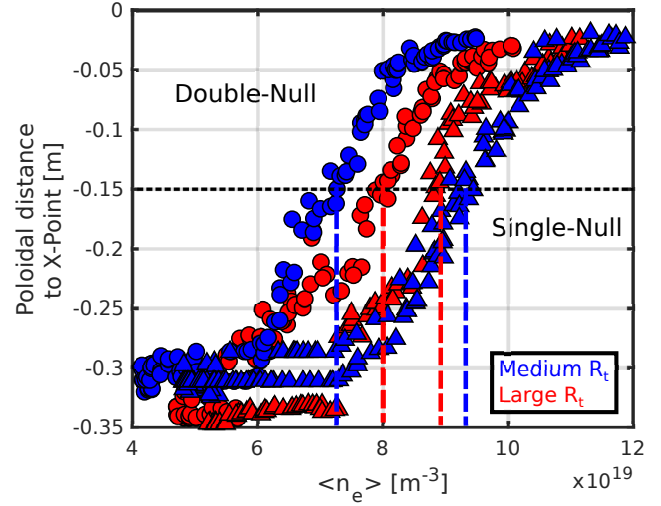


**Figure 15.** Evolution of the CIII front position along the lower outer leg as determined from MANTIS as a function of  $\langle n_e \rangle$ .

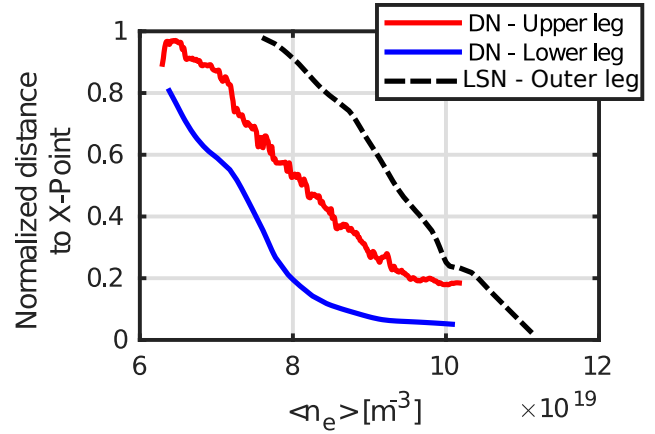


**Figure 16.** Normalized vertical distance between the CIII front position and the X-point in the medium  $R_t$  case ( $I_P = 300$  kA,  $f_x \approx 2.5$ ,  $R_t = 0.76$  m), obtained from a non-tomographic approach.

## 7. References

- [1] T. Eich, A.W. Leonard, R.A. Pitts, W. Fundamenski, R.J. Goldston, T.K. Gray, A. Herrmann, A. Kirk, A. Kallenbach, O. Kardaun, A.S. Kukushkin, B. LaBombard, R. Maingi, M.A. Makowski, A. Scarabosio, B. Sieglin, J. Terry, A. Thornton, ASDEX Upgrade Team, and JET EFDA Contributors. Scaling of the tokamak near the scrape-off layer H-mode power width and implications for ITER. *Nuclear Fusion*, 53(9):093031, 2013.
- [2] A. Loarte, B. Lipschultz, A.S. Kukushkin, G.F. Matthews, P.C. Stangeby, N. Asakura, G.F. Counsell, G. Federici, A. Kallenbach, K. Krieger, A. Mahdavi, V. Philipps, D. Reiter, J. Roth, J. Strachan, D. Whyte, R. Dörner, T. Eich, W. Fundamenski, A. Herrmann, M. Fenstermacher, P. Ghendrih, M. Groth, A. Kirschner, S. Konoshima, B. LaBombard, P. Lang, A.W. Leonard, P. Monier-Garbet, R. Neu, H. Pacher, B. Pegourie, R.A. Pitts, S. Takamura, J. Terry, E. Tsimone, the ITPA Scrape-off Layer, and Divertor Physics Topical Group. Chapter 4: Power and particle control. *Nuclear Fusion*,

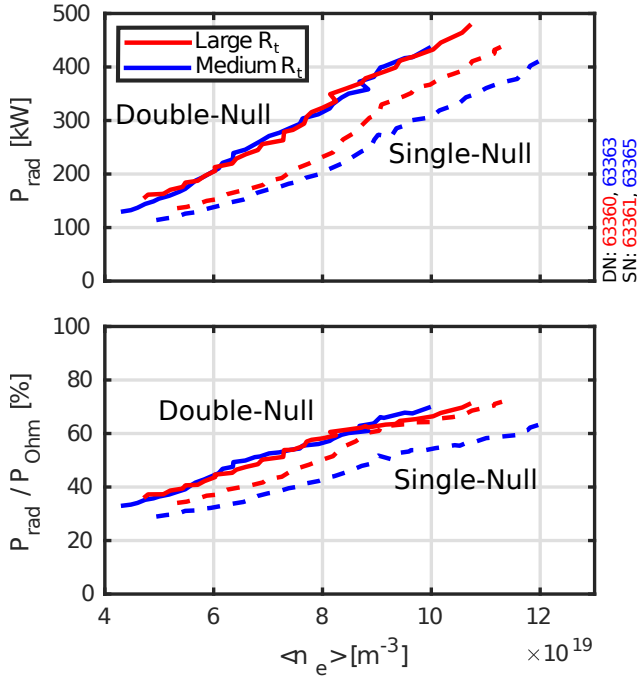


**Figure 17.** Total radiated power  $P_{rad}$  (top panel) and normalized radiated power (lower panel) for LSN (dashed lines) and DN (solid lines) configurations in the medium (blue lines) and large  $R_t$  (red lines) cases.

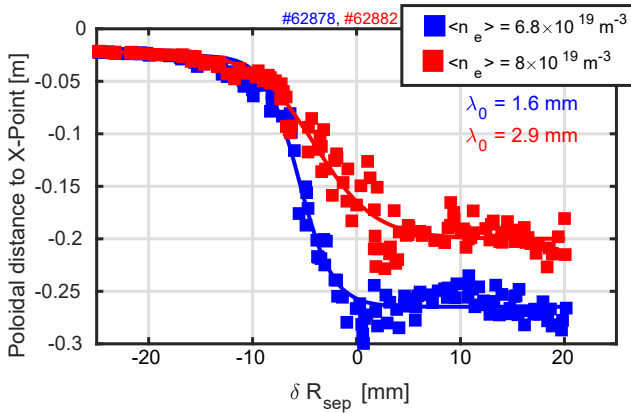


**Figure 18.** Position of the CIII front location along the lower outer leg of a DN-SX plasma as  $\delta R_{sep}$  is varied. The blue squares correspond to a strongly attached plasma ( $\langle n_e \rangle = 6.8 \times 10^{19} m^{-3}$ ). The red squares corresponds to a slightly detached plasma ( $\langle n_e \rangle = 8 \times 10^{19} m^{-3}$ ). The solid lines correspond to fit of the data points with a logistic function described by equation 1.

- 47(6):S203, 2007.
- [3] H. Zohm, C. Angioni, E. Fable, G. Federici, G. Gantenbein, T. Hartmann, K. Lackner, E. Poli, L. Porte, O. Sauter, G. Tardini, D. Ward, and M. Wischmeier. On the physics guidelines for a tokamak DEMO. *Nuclear Fusion*, 53(7):073019, jun 2013.
  - [4] R. A. Pitts, X. Bonnin, F. Escourbiac, H. Frerichs, J. P. Gunn, T. Hirai, A. S. Kukushkin, E. Kaveeva, M. A. Miller, D. Moulton, V. Rozhansky, I. Senichenkov, E. Sytova, O. Schmitz, P. C. Stangeby, G. De Temmerman, I. Veselova, and S. Wiesen. Physics basis for the first ITER tungsten divertor. *Nuclear Materials and Energy*, 20:100696, aug 2019.
  - [5] M. Wischmeier. High density operation for reactor-relevant power exhaust. *Journal of Nuclear Materials*, 463:22 – 29, 2015.
  - [6] H. Reimerdes, R. Ambrosino, P. Innocente, A. Castaldo, P. Chmielewski, G. Di Gironimo, S. Merriman, V. Pericoli-Ridolfini, L. Aho-Mantilla, R. Albanese, et al. Assessment of alternative divertor configurations as an exhaust solution for DEMO. *Nuclear Fusion*, 60(6):066030, 2020.
  - [7] P.C. Stangeby. *The Plasma Boundary of Magnetic Fusion Devices*. Series in Plasma Physics and Fluid Dynamics. Taylor & Francis, 2000.
  - [8] S. I. Krasheninnikov, A. S. Kukushkin, and A. A. Pshenov. Divertor plasma detachment. *Physics of Plasmas*, 23(5):055602, 2016.
  - [9] A W Leonard. Plasma detachment in divertor tokamaks. *Plasma Physics and Controlled Fusion*, 60(4):044001, feb 2018.
  - [10] C. Theiler, B. Lipschultz, J. Harrison, B. Labit, H. Reimerdes, C. Tsui, W.A.J. Vijvers, J. A. Boedo, B.P. Duval, S. Elmore, P. Innocente, U. Kruezi, T. Lunt, R. Maurizio, F. Nespoli, U. Sheikh, A.J. Thornton, S.H.M. van Limpt, K. Verhaegh, and N. Vianello and. Results from recent detachment experiments in alternative divertor configurations on TCV. *Nuclear Fusion*, 57(7):072008, mar 2017.
  - [11] B. Lipschultz, B. LaBombard, J. L. Terry, C. Boswell, and I. H. Hutchinson. Divertor physics research on Alcator C-Mod. *Fusion Science and Technology*, 51(3):369–389, 2007.
  - [12] P. M. Valanju, M. Kotschenreuther, S. M. Mahajan, and J. Canik. Super-X divertors and high power density fusion devices. *Physics of Plasmas*, 16(5), 2009.
  - [13] M. Kotschenreuther, P. M. Valanju, S. M. Mahajan, and J. C. Wiley. On heat loading, novel divertors, and fusion reactors. *Physics of Plasmas*, 14(7), 2007.
  - [14] D. D. Ryutov. Geometrical properties of a "snowflake" divertor. *Physics of Plasmas*, 14(6), 2007.
  - [15] G. Federici, C. Bachmann, L. Barucca, W. Biel, L. Boccaccini, R. Brown, C. Bustreo, S. Ciattaglia, F. Cismondi, M. Coleman, V. Corato, C. Day, E. Diegele, U. Fischer, T. Franke, C. Gliss, A. Ibarra, R. Kembleton, A. Loving, F. Maviglia, B. Meszaros, G. Pintsuk, N. Taylor, M.Q. Tran, C. Vorpahl, R. Wenninger, and J.H. You. Demo design activity in europe: Progress and updates. *Fusion Engineering and Design*, 136:729–741, 2018. Special Issue: Proceedings of the 13th International Symposium on Fusion Nuclear Technology (ISFNT-13).
  - [16] R. Ambrosino, A. Castaldo, S. Ha, V.P. Loschiavo, S. Merriman, and H. Reimerdes. Evaluation of feasibility and costs of alternative magnetic divertor configurations for DEMO. *Fusion Engineering and Design*, 146:2717 – 2720, 2019. SI:SOFT-30.
  - [17] K. Im, S. Kwon, and J. S. Park. A Preliminary Development of the K-DEMO Divertor Concept. *IEEE Transactions on Plasma Science*, 44(10):2493–2501, Oct 2016.

- [18] A.Q. Kuang, N.M. Cao, A.J. Creely, C.A. Dennett, J. Hecla, B. LaBombard, R.A. Tinguely, E.A. Tolman, H. Hoffman, M. Major, J. Ruiz Ruiz, D. Brunner, P. Grover, C. Laughman, B.N. Sorbom, and D.G. Whyte. Conceptual design study for heat exhaust management in the ARC fusion pilot plant. *Fusion Engineering and Design*, 137:221–242, 2018.
- [19] D. Brunner, A. Q. Kuang, B. Labombard, and J. L. Terry. The dependence of divertor power sharing on magnetic flux balance in near double-null configurations on Alcator C-Mod. *Nuclear Fusion*, 58(7):076010, may 2018.
- [20] T.W. Petrie, C.M. Greenfield, R.J. Grobener, A.W. Hyatt, R.J. La Haye, A.W. Leonard, M.A. Mahdavi, T.H. Osborne, M.J. Schaffer, D.M. Thomas, W.P. West, S.L. Allen, M.E. Fenstermacher, C.J. Lasnier, G.D. Porter, N.S. Wolf, J.G. Watkins, and T.L. Rhodes. The effect of divertor magnetic balance on H-mode performance in DIII-D. *Journal of Nuclear Materials*, 290-293:935–939, 2001. 14th Int. Conf. on Plasma-Surface Interactions in Controlled Fusion D evices.
- [21] T.W. Petrie, N.H. Brooks, M.E. Fenstermacher, M. Groth, A.W. Hyatt, R.C. Isler, C.J. Lasnier, A.W. Leonard, G.D. Porter, M.J. Schaffer, J.G. Watkins, M.R. Wade, and W.P. West. Comparison of radiating divertor behaviour in single-null and double-null plasmas in DIII-D. *Nuclear Fusion*, 48(4):045010, mar 2008.
- [22] T. W. Petrie, B. Grierson, T. H. Osborne, F. Turco, S. L. Allen, M. E. Fenstermacher, J. R. Ferron, H. Y. Guo, E. Hinson, R. La Haye, C. J. Lasnier, A. W. Leonard, T. C. Luce, C. Petty, D. Thomas, B. Victor, H. Wang, and J. G. Watkins. High-performance double-null plasmas under radiating mantle scenarios on DIII-D. *Nuclear Materials and Energy*, 19:267–272, may 2019.
- [23] H.Y. Guo, X. Gao, J. Li, G.-N. Luo, S. Zhu, J.F. Chang, Y.P. Chen, W. Gao, X.Z. Gong, Q.S. Hu, Q. Li, S.C. Liu, T.F. Ming, J. Ou, Y.J. Shi, B.N. Wan, D.S. Wang, H.Q. Wang, J. Wang, Z.W. Wu, B.J. Xiao, Q. Xu, L. Zhang, and W. Zhang. Recent progress on divertor operations in EAST. *Journal of Nuclear Materials*, 415(1, Supplement):S369–S374, 2011. Proceedings of the 19th International Conference on Plasma-Surface Interactions in Controlled Fusion.
- [24] G. De Temmerman, E. Delchambre, J. Dowling, A. Kirk, S. Lisgo, and P. Tamain. Thermographic study of heat load asymmetries during MAST L-mode discharges. *Plasma Physics and Controlled Fusion*, 52(9):095005, jul 2010.
- [25] S. Coda, M. Agostini, R. Albanese, S. Alberti, E. Alessi, S. Allan, J. Allcock, R. Ambrosino, H. Anand, Y. Andrébe, H. Arnichand, F. Auriemma, J.M. Ayllon-Guerola, F. Bagnato, J. Ball, M. Baquero-Ruiz, A.A. Beletskii, M. Bernert, W. Bin, P. Blanchard, T.C. Blanken, J.A. Boedo, O. Bogar, T. Bolzonella, F. Bombarda, N. Bonanomi, F. Bouquey, C. Bowman, D. Brida, J. Bucalossi, J. Buermans, H. Bufferand, P. Buratti, G. Calabró, L. Calacci, Y. Camenen, D. Carnevale, F. Carpanese, M. Carr, L. Carraro, A. Casolari, F. Causa, J. Čeřovský, O. Chellaï, P. Chmielewski, D. Choi, N. Christen, G. Ciraolo, L. Cordaro, S. Costea, N. Cruz, A. Czarnicka, A. Dal Molin, P. David, J. Decker, H. De Oliveira, D. Douai, M.B. Dreval, B. Dudson, M. Dunne, B.P. Duval, T. Eich, S. Elmore, O. Embréus, B. Esposito, M. Faitsch, M. Farnik, A. Fasoli, N. Fedorczak, F. Felici, S. Feng, X. Feng, G. Ferró, O. Février, O. Ficker, A. Fil, M. Fontana, L. Frassinetti, I. Furno, D.S. Gahle, D. Galassi, K. Galkazka, A. Gallo, C. Galperti, S. Garavaglia, J. Garcia, M. Garcia-Muñoz, A.J. Garrido, I. Garrido, J. Gath, B. Geiger, G. Giruzzi, M. Gobbin, T.P. Goodman, G. Gorini, M. Gospodarczyk, G. Granucci, J.P. Graves, M. Gruca, T. Gyergyek, A. Hakola, T. Happel, G.F. Harrer, J. Harrison, E. Havlíčková, J. Hawke, S. Henderson, P. Hennequin, L. Hesslow, D. Hogewei, J.-Ph. Hogge, C. Hopf, M. Hoppe, J. Horáček, Z. Huang, A. Hubbard, A. Iantchenko, V. Igochine, P. Innocente, C. Ionita Schrittwieser, H. Isliker, R. Jacquier, A. Jardin, A. Kappatou, A. Karpushov, P.-V. Kazantzidis, D. Keeling, N. Kirneva, M. Komm, M. Kong, J. Kovacic, N. Krawczyk, O. Kudlacek, T. Kurki-Suonio, R. Kwiatkowski, B. Labit, E. Lazzaro, B. Linehan, B. Lipschultz, X. Llobet, R. Lombroni, V.P. Loschiavo, T. Lunt, E. Macusova, J. Madsen, E. Maljaars, P. Mantica, M. Maraschek, C. Marchetto, A. Marco, A. Mariani, C. Marini, Y. Martin, F. Matos, R. Maurizio, B. Mavkov, D. Mazon, P. McCarthy, R. McDermott, V. Menkovski, A. Merle, H. Meyer, D. Micheletti, F. Militello, K. Mitosinkova, J. Mlynář, V. Moiseenko, P.A. Molina Cabrera, J. Morales, J.-M. Moret, A. Moro, R.T. Mumgaard, V. Naulin, R.D. Nem, F. Nespoli, A.H. Nielsen, S.K. Nielsen, M. Nocente, S. Nowak, N. Offeddu, F.P. Orsitto, R. Paccagnella, A. Palha, G. Papp, A. Pau, R.O. Pavlichenko, A. Perek, V. Pericoli Ridolfini, F. Pecosca, V. Piergotti, L. Pigatto, P. Piovesan, C. Piron, V. Plyusnin, E. Poli, L. Porte, G. Pucella, M.E. Puiatti, T. Pütterich, M. Rabinski, J. Juul Rasmussen, T. Ravensbergen, M. Reich, H. Reimerdes, F. Reimold, C. Reux, D. Ricci, P. Ricci, N. Rispoli, J. Rosato, S. Saarelma, M. Salewski, A. Salmi, O. Sauter, M. Schefler, Ch. Schlatter, B.S. Schneider, R. Schrittwieser, S. Sharapov, R.R. Sheeba, U. Sheikh, R. Shousha, M. Silva, J. Sinha, C. Sozzi, M. Spolaore, L. Stipani, P. Strand, T. Tala, A.S. Tema Biwole, A.A. Teplukhina, D. Testa, C. Theiler, A. Thornton, G. Tomaž, M. Tomes, M.Q. Tran, C. Tsironis, C.K. Tsui, J. Urban, M. Valisa, M. Vallar, D. Van Vugt, S. Vartanian, O. Vasilovici, K. Verhaegh, L. Vermare, N. Vianello, E. Viezzer, W.A.J. Vijvers, F. Villone, I. Voitsekhoitch, N.M.T. Vu, N. Walkden, T. Wauters, M. Weiland, H. Weisen, M. Wensing, M. Wiesenberger, G. Wilkie, M. Wischmeier, K. Wu, M. Yoshida, R. Zagorski, P. Zanca, J. Zebrowski, A. Zisis, and M. Zuin and. Physics research on the TCV tokamak facility: from conventional to alternative scenarios and beyond. *Nuclear Fusion*, 59(11):112023, aug 2019.
- [26] A. Fasoli, H. Reimerdes, S. Alberti, M. Baquero-Ruiz, B.P. Duval, E. Havlikova, A. Karpushov, J.-M. Moret, M. Toussaint, H. Elaian, M. Silva, C. Theiler, and D. Vaccaro and. TCV heating and divertor upgrades. *Nuclear Fusion*, 60(1):016019, nov 2019.
- [27] H. Reimerdes, B.P. Duval, H. Elaian, A. Fasoli, O. Février, C. Theiler, F. Bagnato, M. Baquero-Ruiz, P. Blanchard, D. Brida, C. Colandrea, H. De Oliveira, D. Galassi, S. Gorno, S. Henderson, M. Komm, B. Linehan, L. Martinelli, R. Maurizio, J.-M. Moret, A. Perek, H. Raj, U. Sheikh, D. Testa, M. Toussaint, C.K. Tsui, M. Wensing, the TCV team, and the EUROfusion MST1 team. Initial TCV operation with a baffled divertor. *Nuclear Fusion*, 61(2):024002, jan 2021.
- [28] R.A. Pitts, B.P. Duval, A. Loarte, J.-M. Moret, J.A. Boedo, D. Coster, I. Furno, J. Horacek, A.S. Kukushkin, D. Reiter, and J. Rommers. Divertor geometry effects on detachment in TCV. *Journal of Nuclear Materials*, 290(Supplement C):940 – 946, 2001. 14th Int. Conf. on Plasma-Surface Interactions in Controlled Fusion Devices.
- [29] O. Février, C. Theiler, H. De Oliveira, B. Labit, N. Fedorczak, and A. Bailod. Analysis of wall-embedded langmuir probe signals in different conditions on the Tokamak à Configuration Variable. *Review of Scientific Instruments*, 89(5):053502, 2018.

- [30] H. De Oliveira, P. Marmillod, C. Theiler, R. Chavan, O. Février, B. Labit, P. Lavanchy, B. Marlétaz, and R. A. Pitts. Langmuir probe electronics upgrade on the Tokamak à Configuration Variable. *Review of Scientific Instruments*, 90(8):083502, 2019.
- [31] H. Arnichand, Y. Andrebe, P. Blanchard, S. Antonioni, S. Couturier, J. Decker, B.P. Duval, F. Felici, C. Galperti, P.-F. Isoz, P. Lavanchy, X. Llobet, B. Marlétaz, P. Marmillod, and J. Masur. New capabilities of the incoherent thomson scattering diagnostics in the TCV tokamak: divertor and real-time measurements. *Journal of Instrumentation*, 14(09):C09013–C09013, sep 2019.
- [32] R. Maurizio, S. Elmore, N. Fedorczak, A. Gallo, H. Reimerdes, B. Labit, C. Theiler, C.K. Tsui, W.A.J. Vijvers, The TCV Team, and The MST1 Team. Divertor power load studies for attached L-mode single-null plasmas in TCV. *Nuclear Fusion*, 58(1):016052, 2018.
- [33] B. L. Linehan, R. T. Mumgaard, M. Wensing, K. Verhaegh, Y. Andrebe, J. R. Harrison, B. P. Duval, and C. Theiler. The multi-spectral imaging diagnostic. *Review of Scientific Instruments*, 89(10):103503, 2018.
- [34] A. Perek, W. A. J. Vijvers, Y. Andrebe, I. G. J. Classen, B. P. Duval, C. Galperti, J. R. Harrison, B. L. Linehan, T. Ravensbergen, K. Verhaegh, and M. R. de Baar. MANTIS: A real-time quantitative multispectral imaging system for fusion plasmas. *Review of Scientific Instruments*, 90(12):123514, 2019.
- [35] J.R. Harrison, W.A.J. Vijvers, C. Theiler, B.P. Duval, S. Elmore, B. Labit, B. Lipschultz, S.H.M. van Limpt, S.W. Lisgo, C.K. Tsui, H. Reimerdes, U. Sheikh, K.H.A. Verhaegh, and M. Wischmeier. Detachment evolution on the TCV tokamak. *Nuclear Materials and Energy*, 12:1071 – 1076, 2017. Proceedings of the 22nd International Conference on Plasma Surface Interactions 2016, 22nd PSI.
- [36] O. Février, H. Reimerdes, C. Theiler, D. Brida, C. Colandrea, H. De Oliveira, B.P. Duval, D. Galassi, S. Gorno, S. Henderson, M. Komm, B. Labit, B. Linehan, L. Martinelli, A. Perek, H. Raj, U. Sheikh, C.K. Tsui, and M. Wensing. Divertor closure effects on the TCV boundary plasma. *Nuclear Materials and Energy*, 27:100977, 2021.
- [37] J.-M. Moret, B.P. Duval, H.B. Le, S. Coda, F. Felici, and H. Reimerdes. Tokamak equilibrium reconstruction code LIUQE and its real time implementation. *Fusion Engineering and Design*, 91(Supplement C):1 – 15, 2015.
- [38] Carrie Fiona Beadle. *Turbulence in the scrape-off layer of double-null tokamak configurations*. PhD thesis, Lausanne, 2021.
- [39] R. Maurizio, B.P. Duval, B. Labit, H. Reimerdes, M. Faitsch, M. Komm, U. Sheikh, C. Theiler, and the TCV team and. H-mode scrape-off layer power width in the TCV tokamak. *Nuclear Fusion*, 61(2):024003, jan 2021.
- [40] V A Soukhanovskii. A review of radiative detachment studies in tokamak advanced magnetic divertor configurations. *Plasma Physics and Controlled Fusion*, 59(6):064005, apr 2017.
- [41] A Fil, B Lipschultz, D Moulton, B D Dudson, O Février, O Myatra, C Theiler, K Verhaegh, M Wensing, and and. Separating the roles of magnetic topology and neutral trapping in modifying the detachment threshold for TCV. *Plasma Physics and Controlled Fusion*, 62(3):035008, jan 2020.
- [42] R. Maurizio, B.P. Duval, B. Labit, H. Reimerdes, C. Theiler, C.K. Tsui, J. Boedo, H. De Oliveira, O. Février, U. Sheikh, M. Spolaore, K. Verhaegh, N. Vianello, and M. Wensing. Conduction-based model of the Scrape-Off Layer power sharing between inner and outer divertor in diverted low-density tokamak plasmas. *Nuclear Materials and Energy*, 19:372 – 377, 2019.
- [43] C. Theiler, A.J. Thornton, C. Colandrea, H. De Oliveira, B. Duval, O. Février, A. Fil, D. Galassi, S. Gorno, J. Harrison, B. Labit, B. Linehan, B. Lipschultz, L. Martinelli, R. Maurizio, A. Perek, H. Reimerdes, U. Sheikh, C. Tsui, K. Verhaegh, M. Wensing, the TCV Team, and the EUROfusion MST1 Team. Baffled and non-baffled Super-X studies on TCV. In *3rd IAEA Technical Meeting on Divertor Concepts*, November 2019.
- [44] O Février, C Theiler, J R Harrison, C K Tsui, K Verhaegh, C Wüthrich, J A Boedo, H De Oliveira, B P Duval, B Labit, B Lipschultz, R Maurizio, H Reimerdes, and and. Nitrogen-seeded divertor detachment in TCV L-mode plasmas. *Plasma Physics and Controlled Fusion*, 62(3):035017, feb 2020.
- [45] G. Fishpool, J. Canik, G. Cunningham, J. Harrison, I. Katramados, A. Kirk, M. Kovari, H. Meyer, and R. Scannell. MAST-upgrade divertor facility and assessing performance of long-legged divertors. *Journal of Nuclear Materials*, 438:S356 – S359, 2013. Proceedings of the 20th International Conference on Plasma-Surface Interactions in Controlled Fusion Devices.